ADVANCED ELECTRONIC MATERIALS
www.advelectronicmat.de

Sequentially Processed P3HT/CN6-CP$^{\bullet-}$NBu^{4+} Films: Interfacial or Bulk Doping?

*Yevhen Karpov, Nataliya Kiriy, Petr Formanek, Cedric Hoffmann, Tetyana Beryozkina, Mike Hambsch, Mahmoud Al-Hussein, Stefan C. B. Mannsfeld, Bernd Büchner, Bipasha Debnath, Michael Bretschneider, Yulia Krupskaya, Franziska Lissel, and Anton Kiriy**

Derivatives of the hexacyano-[3]-radialene anion radical (CN6-CP$^{\bullet-}$) emerge as a promising new family of p-dopants having a doping strength comparable to that of archetypical dopant 2,3,5,6-tetrafluoro-7,7,8,8-tetracyano-quinodimethane (F4TCNQ). Here, mixed solution (MxS) and sequential processing (SqP) doping methods are compared by using a model semiconductor poly(3-hexylthiophene) (P3HT) and the dopant CN6-CP$^{\bullet-}$NBu$_4^+$ (NBu$_4^+$ = tetrabutylammonium). MxS films show a moderate yet thickness-independent conductivity of ≈0.1 S cm^{-1}. For the SqP case, the highest conductivity value of ≈6 S cm^{-1} is achieved for the thinnest (1.5–3 nm) films whereas conductivity drops two orders of magnitudes for 100 times thicker films. These results are explained in terms of an interfacial doping mechanism realized in the SqP films, where only layers close to the P3HT/dopant interface are doped efficiently, whereas internal P3HT layers remain essentially undoped. This structure is in agreement with transmission electron microscopy, atomic force microscopy, and Kelvin probe force microscopy results. The temperature-dependent conductivity measurements reveal a lower activation energy for charge carriers in SqP samples than in MxS films (79 meV vs 110 meV), which could be a reason for their superior conductivity.

1. Introduction

Over the past decades, organic semiconductors (OSCs) have been extensively investigated due to their tremendous potential for flexible electronics applications.[1] One common way to tune the electronic properties of OSCs is through molecular doping, that is, controlled oxidizing (removal of electrons) or reducing (addition of electrons) the organic semiconductor to create equilibrium charge carriers in otherwise poorly conductive organics.[2,3] Depending on applications, different doping types and regimes are required. For example, distribution of low quantities of dopants in semiconductor layers is desirable for improving the performance of organic field-effect transistors (OFETs).[4–6] Placement of the dopant at the semiconductor–dielectric interface is needed for fabrication of depletion transistors.[7] Heavily doped layers positioned nearby electrodes facilitate the charge-injection and extraction process, thus improving the operation of organic light emitting diodes (OLEDs)[8] and solar cells.[9] Doping has been also shown to be of key importance for thermoelectric devices.[10] The doping of organic semiconductors as a fabrication process has already been implemented in industry, for example in the production of AMOLED displays.[11] Currently, vacuum deposition is predominantly used in industry because it allows a straightforward fabrication of complex multilayered devices with precisely controlled thicknesses and composition by sequential evaporation of different materials (semiconductors, dopants, and emitters).[8] Solution-based technologies have, in general, the potential for cheaper production of large-area devices, however fabrication of multilayers from solutions is still challenging.[12,13]

Dr. Y. Karpov, Dr. N. Kiriy, Dr. P. Formanek, C. Hoffmann, Dr. F. Lissel, Dr. A. Kiriy
Leibniz Institute of Polymer Research Dresden
Hohe Straße 6, Dresden 01069, Germany
E-mail: kiriy@ipfdd.de

Dr. T. Beryozkina
TOSLab
Ural Federal University named after the first President of Russia B. N. Yeltsin
Mira str., 28, Yekaterinburg 620002, Russia

The ORCID identification number(s) for the author(s) of this article can be found under https://doi.org/10.1002/aelm.201901346.

Dr. M. Hambsch, Prof. S. C. B. Mannsfeld
Technische Universität Dresden
Center for Advancing Electronics Dresden (cfaed) and Faculty of Electrical and Computer Engineering
Helmholtzstr. 18, Dresden 01069, Germany

Prof. M. Al-Hussein
Physics Department and Hamdi Mango Center for Scientific Research
The University of Jordan
Amman 11942, Jordan

Prof. B. Büchner, B. Debnath, M. Bretschneider, Dr. Y. Krupskaya
Leibniz Institute for Solid State and Material Research Dresden (IFW)
Helmholtzstraße 20, Dresden 01069, Germany

DOI: 10.1002/aelm.201901346

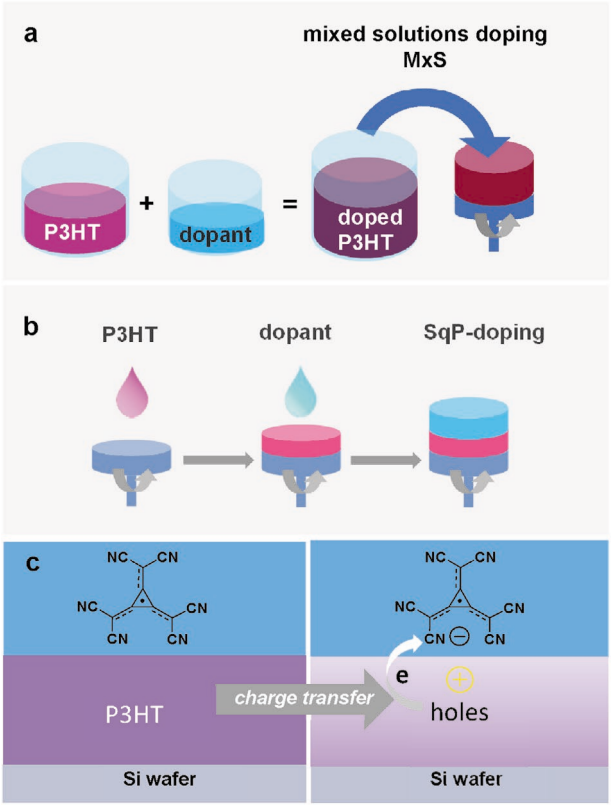

Figure 1. Schematics of a) the mixed solutions and b) sequential processing methods for the doping of P3HT; c) an illustration of an interfacial charge-transfer process.

One of the approaches to overcome this problem is a recently introduced method using sequential processing (SqP) of different components from solvents of different polarity.[14–18] While in the most commonly used mixed-solution (MxS)-doping method (**Figure 1**a), the dopant and the polymer semiconductor are codissolved in a common good solvent (e.g., chloroform) and deposited together,[19–29] SqP involves a stepwise deposition of a semiconducting polymer and a dopant (Figure 1b). The most studies model system comprises the polymer semiconductor poly(3-hexylthiophene) (P3HT) and the dopant 2,3,5,6-tetrafluoro-7,7,8,8-tetracyanoquinodimethane (F4TCNQ). SqP can be achieved by the deposition of the dopant from, for instance, acetonitrile (CH_3CN), which is a nonsolvent for P3HT (Figure 1b).

It was shown that at moderate doping levels, SqP provides somewhat higher conductivity compared to the doped films prepared by the MxS method.[15] Although details of the SqP-doping mechanism are still under extensive discussions, it is believed that the dopant intercalates into the amorphous part of P3HT.[30] To explain the higher doping efficiency of the SqP method under some doping regimes, it was hypothesized that mobile holes, generated in amorphous domains, navigate into crystallites where they have an energetic preference to reside, allowing them to contribute to charge transport while not suffering from ionized dopant scattering.[17] Furthermore, the incorporation of the dopant into amorphous part increases conjugation length of P3HT chains, which contributes to increased conductivity.[17]

Regarding the structure of sequentially doped films, it crucially depends on the dopant and the solvent nature as well as on details of the doping procedure. For instance, when P3HT layers are coated by the F4TCNQ solution in acetonitrile,[17,30] or other solvents,[15] the dopant penetrates deeply into the polymer phase. In contrast, the electrical doping over a limited depth (with a decay constant of 10–20 nm) occurs when more polar dopant/solvent compositions are used, such as a solution of phosphomolybdic acid in nitromethane.[31] As an opposite extreme, the formation of bilayered structures with a spatial separation of dopants and semiconductors was demonstrated in our previous work, when the uncharged F4TCNQ dopant was replaced by the much more polar ionic dopant CN6-CP$^{\bullet-}$K$^+$ (**Figure 2**).[28]

CN6-CP$^{\bullet-}$K$^+$ is a reduction product of CN6-CP, which is a novel p-dopant recently introduced by our group.[29a] Owing to its

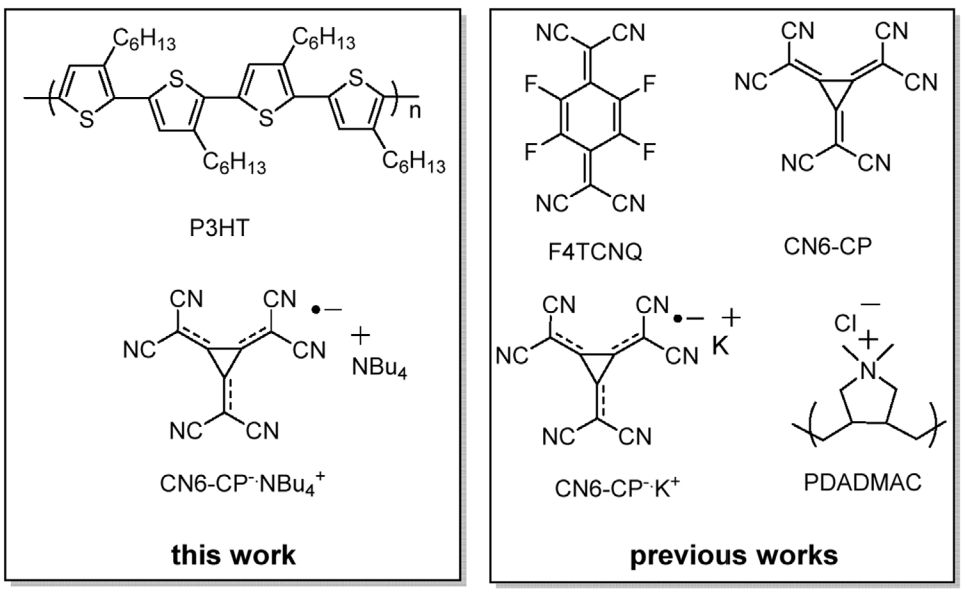

Figure 2. Chemical structures of semiconductors and dopants.

unique [3]-radialene framework and the presence of six electron-deficient cyano-groups, CN6-CP possesses an extremely high electron affinity (EA) of –5.8 eV. Furthermore, its single electron reduction product CN6-CP$^{\bullet-}$K$^+$ also acts as a p-dopant having an EA of –5.1 eV, comparable with the EA of F4TCNQ.[29b] An attractive feature of CN6-CP$^{\bullet-}$ salts is their high thermal and environmental stability, unusual for free radicals, and excellent solubility, which can be easily tuned by variation of the nature of the counterion. CN6-CP$^{\bullet-}$K$^+$ can be synthesized in multigram quantities in two easy steps and a number of other CN6-CP$^{\bullet-}$ salts, such as one soluble in organics by using tetra-alkyl ammonium can be prepared via experimentally simple ion-exchange reactions.[29b] On the other hand, the negative charge of CN6-CP$^{\bullet-}$ can be used for its immobilization onto the oppositely charged PDADMAC layer deposited on top of P3HT films. It was shown that the deposition of CN6-CP$^{\bullet-}$K$^+$ onto a P3HT/PDADMAC bilayer leads to the layered structure P3HT/PDADMAC/CN6-CP$^{\bullet-}$ with no observable penetration of the dopant into the polymer.[28] Despite the spatial separation of the dopant and the semiconductor layer, the efficiency of this interfacial kind of doping was high, especially for thin films and conductivities in the 5–13 S cm^{-1} range were achieved for P3HT films with a thickness of a few nanometers. We proposed that penetration of the dopant into P3HT is prohibited because of the high polarity of the dopant CN6-CP$^{\bullet-}$K$^+$ and the solvent (methanol). In addition, the polycation interlayer forms an insoluble complex with the dopant, which may play a role as a protective barrier.

The present work further explores the doping ability of the CN6-CP$^{\bullet-}$ anion-radicals. Particularly, it investigates sequential doping of P3HT in the absence of the polycation interlayer by using a rather hydrophobic CN6-CP$^{\bullet-}$NBu$_4^+$ salt, which is highly soluble in various organic solvents due to the presence of a bulky organic counterion. In contrast to CN6-CP$^{\bullet-}$K$^+$, CN6-CP$^{\bullet-}$NBu^{4+} is soluble in both common and orthogonal solvents for P3HT, making it possible to apply and compare efficiencies of the MxS- and SqP-doping methods by using the same dopant. Thus, by using this dopant, it is possible to verify the generality of the trend established for the P3HT/F4TCNQ system, namely, that SqP enables higher efficiency at moderate doping regimes than the MxS.

2. Results

2.1. Electrical Conductivity

Electrical measurements were performed by two-probe method by using devices with interdigitated electrodes and having different channel dimensions (200 µm × 0.45 mm and 300 µm × 11 mm). We start with conductivity measurements of MxS-doped films. In addition, temperature-dependent electrical measurements were performed for 4-probe devices. Although the MxS-doping was already reported in our recent paper, we repeated some of the experiments to obtain data from the same polymer batch and to study the dependence of the conductivity on the thickness of the doped films and results are provided in Table S1 in the Supporting Information. **Figure 3**a (black squares) shows the dependence of the resistance (R) on the thickness of MxS-doped P3HT films, at a constant molar doping ratio, MDR = [CN6-CP$^{\bullet-}$NBu$_4^+$]/[3HT] = 0.3.

This MDR was previously identified as the optimal value for achieving the highest conductivity.[29b] The resistance follows a reciprocal dependence on the thickness for n varied in a range from 11 to 150 nm (Figure 3a). This is characteristic for a material having homogeneous properties and a constant specific conductivity.

To study the SqP-doping, P3HT films with the thickness varied from 1.5 to 250 nm were prepared. According to atomic force microscopy (AFM) and ellipsometry data, the thinnest P3HT film from this series represents a discontinuous P3HT monolayer. Atop of the polymer films, a solution of CN6-CP$^{\bullet-}$NBu$_4^+$ in ethanol with a concentration of 10 g L^{-1} was spin coated. With this dopant concentration and spin-coating conditions, a full and homogeneous coverage of P3HT films with at least 20 nm thick dopant layer was provided, as verified by AFM (**Figure 4**a). The full coverage of the samples with the dopant was provided to ensure excessive amounts of the dopant. In this case, penetration of the dopant inside the polymer phase is not limited by the amount of available dopant for the doping even for the thickest P3HT film. As seen in Figure 3a (red circles),

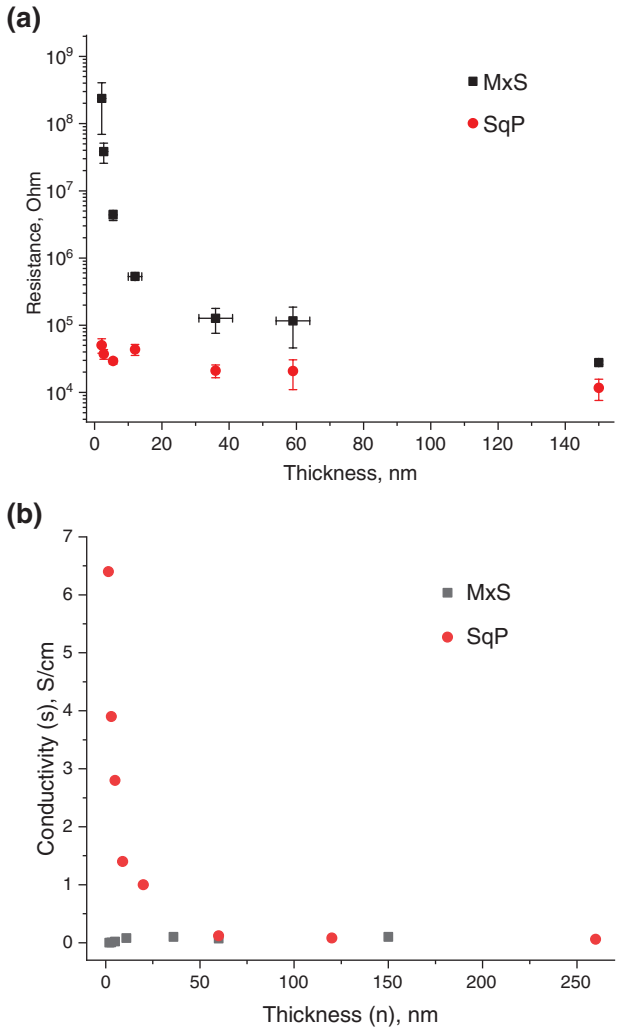

Figure 3. Dependencies of a) resistance and b) conductivity on the thickness for P3HT/CN6-CP$^{\bullet-}$NBu$_4^+$ films doped by MxS (black squares) and SqP (red circles) methods.

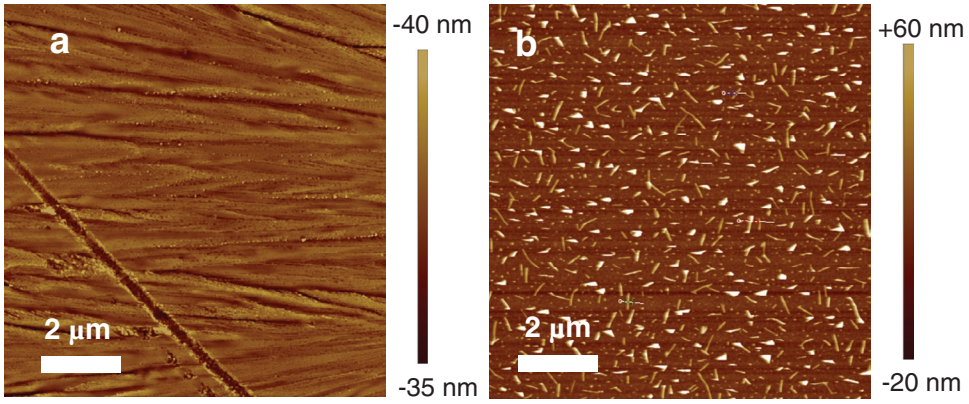

Figure 4. AFM topography images of SqP-doped P3HT/CN6-CP$^{\bullet-}$NBu$_4^+$ films prepared at a) 10 g L^{-1} and b) 1 g L^{-1} dopant concentrations.

the resistance of the doped samples undergoes little changes in a broad range of thicknesses from 1.5 to 250 nm suggesting a very limited penetration of the dopant into the polymer. Indeed, if the dopant freely penetrates into the polymer phase, the resistance should follow the inversely proportional dependence of the film thickness, which is not the case. Furthermore, the fact that the samples with thicknesses varied by two orders of magnitude possess a comparable resistance suggests that all of them have similar dopant penetration depths, which are close to the thickness of the thinnest sample (i.e., close to 1.5 nm). Hence, these measurements demonstrate that the SqP-doped films have a layered structure and involve an interfacial doping mechanism.

To study the influence of the amount of dopant on the SqP-doping process, a series of P3HT films with the thickness fixed to 20 nm was prepared and then, solutions of CN6-CP$^{\bullet-}$NBu$_4^+$ in ethanol with concentrations varied from 0.1 to 30 g L^{-1}, were spin-coated. The resistance of the SqP-doped samples dropped from ≈1 GΩ for pristine P3HT film (Table S1, entry 1, Supporting Information) to R = 275 kΩ at 1 g L^{-1} (entry 10) and leveling at the dopant concentration of 10 g L^{-1} (R = 41 kΩ for 10 g L^{-1} and to R = 37 kΩ for 30 g L^{-1}, entries 11 and 12). These values correspond to conductivities varying from 10^{-5} S cm^{-1} for undoped films to 0.3–0.5 S cm^{-1} for films treated with 10 g L^{-1} dopant solution. AFM measurements show that at low concentrations (e.g., for 1 g L^{-1}, Figure 4b), the films are not fully covered with the dopant but segregates forming 10–30 nm thick and micrometer-long nanorods as well as smaller round-shaped objects. Quantitative processing of the AFM data shows that these nanostructures occupy ≈13% of the whole surface at the dopant concentration of 1 g L^{-1} (Figure 4b). Interestingly, resistances of the samples correlate well with the coverage degree of the surface with the dopant. For example, at full surface coverage, such as at 10 and 30 g L^{-1} concentrations (Figure 4a), resistance is constant (39 kΩ); when the coverage drops by a factor of 6.7 (from 96% for to 13% for 1 g L^{-1}), the resistance increases by a factor of 7.4. These data are in excellent agreement with the interfacial doping mechanism according to which only the dopant segregated atop of the polymer, but not the dopant penetrated into the polymer phase, contributes to the doping and conductivity increase.

It is interesting to compare conductivities achievable by the two methods. MxS-doped samples in the 11–150 nm thickness range exhibit $\sigma \approx$ 0.1 S cm^{-1} and a weak conductivity/thickness dependence (Table S1, entries 2–5, Supporting Information), which is characteristic for homogeneous materials, such as P3HT with evenly distributed dopant. A significant drop of the conductivity (1–2 orders of magnitude; Table S1, entries 6–8, Supporting Information) for ultrathin films (<5 nm) can provisionally be explained in terms of percolation theory suggesting that the size of individual conductive pathways in MxS-doped films is comparable with the thickness of the film at which a significant drop of the conductivity is observed (i.e., at ≈5 nm). This point might correspond to a transition from the 3D to 2D regime accompanied with an abrupt conductivity decrease.

The conductivity of SqP-doped films calculated under assumption that films are homogeneously doped gives the highest conductivity of 6–7 S cm^{-1} for the thinnest P3HT film and the conductivity drops with the thickness increase following an inversely proportional dependence (Figure 3b). This dependence for SqP films is consistent with the formation of a layered structure with the dopant located on top of the semiconductor and with minimal intercalation of the dopant into the polymer. The resulting structure can be viewed as a kind of chemical transistor with the dopant layer acting as a top gate, which withdraws electrons from the semiconductor, generating the conductive channel at the dopant/polymer interface and leaving the deep layers undoped. Thus, averaging the conductivity of highly conductive topmost layers and less conductive bottom layers accounts to strongly thickness-dependent conductivity values for the SqP-doped samples.

Temperature-dependent electrical measurements were performed to get better insight into the origin of the superior charge transport in SqP films.[32] Films of MxS and SqP were prepared on glass substrates with Au film electrodes designed for 4-probe measurements allowing to exclude the contact resistance, which is especially crucial at low temperatures. The MxS film was drop cast from a blend solution contained 10 g L^{-1} of P3HT and 5 g L^{-1} of the dopant resulting into ≈4.6 μm thick composite film. To prepare the SqP film, the first layer was drop cast from a 10 g L^{-1} P3HT solution giving a ≈3.1 μm thick P3HT layer. In the second step, the dopant was spin-coated from a 10 g L^{-1} solution in ethanol giving ≈3.2 μm thick resulting film. Thus, the estimated thickness of the second layer is ≈100 nm. The content of P3HT is assumed to be the same for both samples (n = 3.1 μm),

because the P3HT concentration in the precursor solutions was the same in both cases. It should be however emphasized that this estimation is not accurate and allows only a rough comparison of film properties. Geometrical parameters for the two samples are as follow: the channel length, l, is 3.1 mm in both cases, the distance between 4-probe electrodes is 0.9 mm, and the channel width, W, is 3.7 mm and 4.1 mm for SqP and MxS, respectively. Compared to MxS films, the SqP sample exhibits a much lower resistance at room temperature (R_{SqP} = 18 kΩ vs R_{MxS} = 96 kΩ), in agreement with the above discussed data, and an even larger difference is observed at T = 61 K (R_{SqP} = 1 GΩ; R_{MxS} = 27 GΩ). The 2-probe and 4-probe measurements showed similar resistivity values indicating negligible contact resistance. Both films show thermally activated charge transport, $R \sim \exp(E_a/k_BT)$ (see **Figure 5**) where E_a is the activation energy and k_B is Boltzmann constant. The lower activation energy E_a = 79 meV of the SqP film, compared to 110 meV in the MxS film, assuming comparable density of states in P3HT, leads to higher charge carrier density at a given temperature, which would explain the higher conductance of SqP films.

2.2. Transmission Electron Microscopy (TEM) Studies

To verify the conclusions made on the basis of the electrical measurements about the layered structure of SqP films, morphological and structural investigations were undertaken. For TEM studies, a ≈100 nm thick P3HT film was prepared by spin-coating on a silicon wafer and then a drop of CN6-CP$^{\bullet-}$NBu$_4^+$ in ethanol was placed and allowed to evaporate. Afterward, a cross-section of the resulting film was made by focused ion beam (FIB) and the resulting lamella was investigated by TEM.

Figure 6a shows TEM images of the cross-section nearby the dopant droplet edge. The TEM image confirms the layered structure of the cross-section. The most valuable information comes from element mapping of the cross-section with energy filtered TEM (EF-TEM; Figure 6b). As the dopant is a nitrogen-rich compound whereas P3HT contains no nitrogen but sulfur instead, the two materials have a good EF-TEM contrast. Figure 6b clearly proves the layered structure and the absence of the infiltration of the dopant into the polymer phase. In contrast, a control cross-section of P3HT&CN6-CP$^{\bullet-}$NBu$_4^+$ prepared by the MxS method shows homogeneous distribution of components, as expected for the MxS-doped sample.

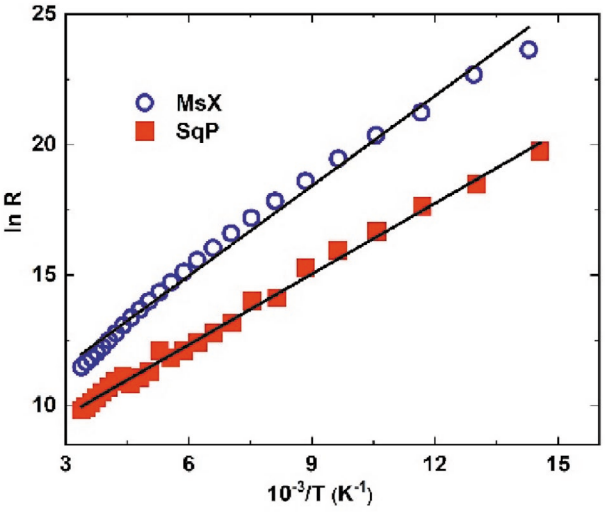

Figure 5. Temperature dependence of R for SqP (red squares) and MxS (blue circles) films measured upon cooling. The black solid lines represent the linear fits performed for the determination of the activation energy E_a (see text for details).

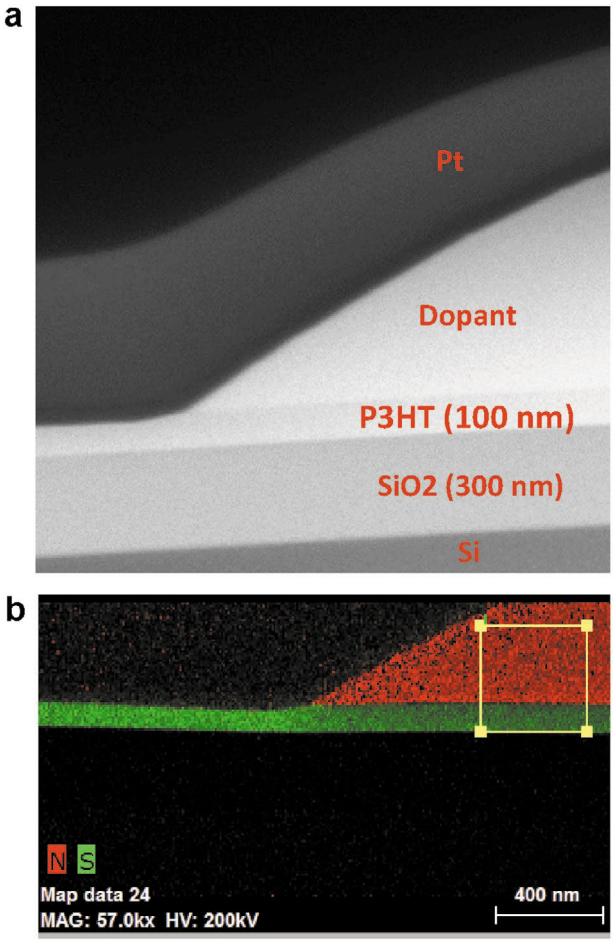

Figure 6. a) TEM image of the FIB-fabricated lamella of a 100 nm thick P3HT layer deposited onto silicon wafer having 300 nm thick silica layer atop of which a drop of CN6-CP$^{\bullet-}$NBu$_4^+$ dopant solution in ethanol was deposited and allowed to evaporate. b) Element mapping of the same sample obtained with energy filtered TEM: distribution of the nitrogen atoms is shown in red and that of sulfur, in green; the image highlights the material contrast and absence of the intermixing of the nitrogen-rich dopant and sulfur-containing polymer.

2.3. Kelvin Probe Force Microscopy (KPFM) Studies

KPFM was used to study the doping process by probing surface potentials (SPs) of the samples. In this work, we used a frequency modulated KPFM (FM-KPFM), which is a tapping mode, single-pass AFM technique which is a particularly convenient method for simultaneous recording of topography and SP images.[32] KPFM is especially relevant to study the doping process, because it probes the

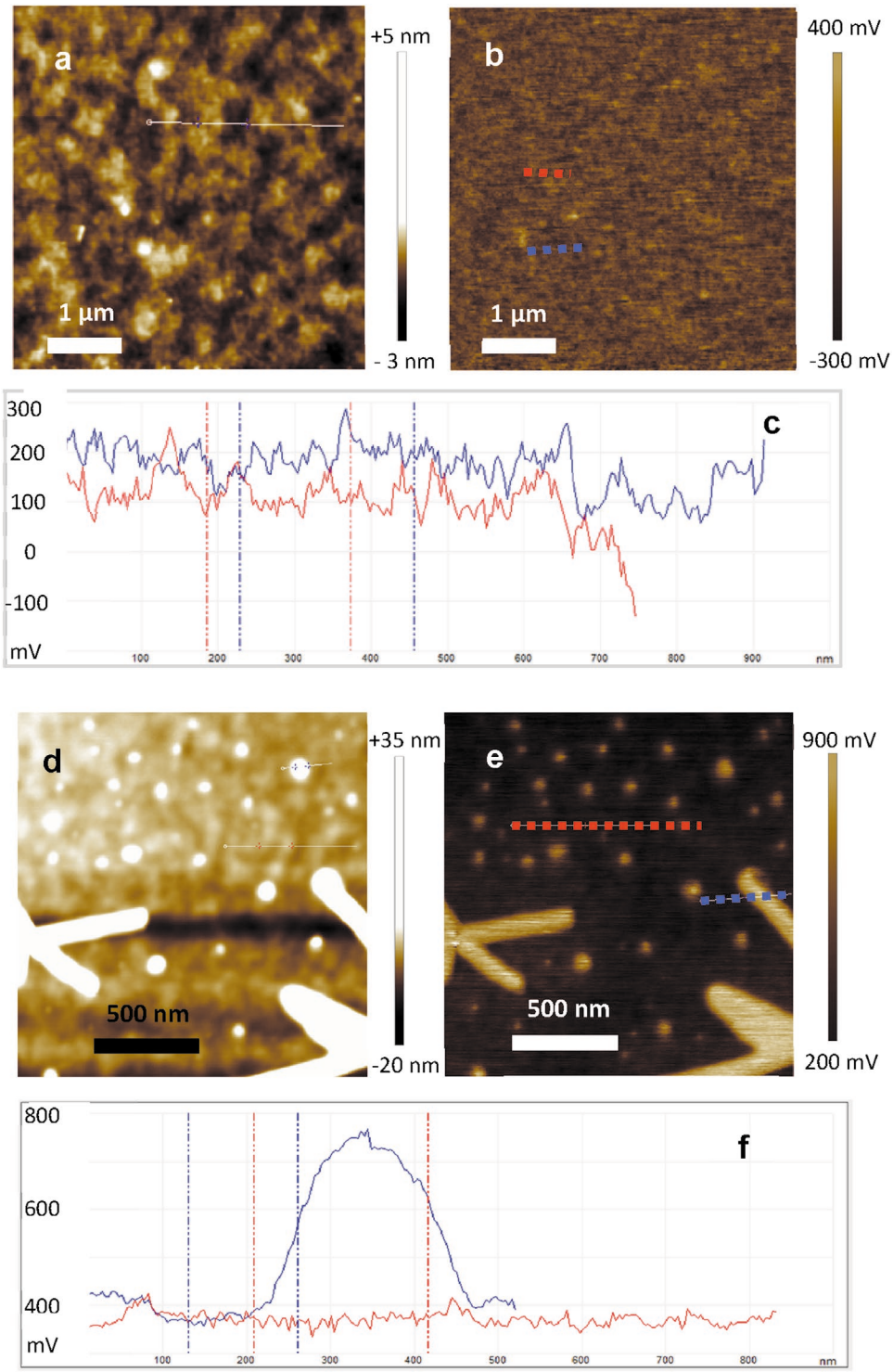

Figure 7. a,d) AFM topography, b,e) SP images and c,f) SP profiles of a–c) a pristine P3HT film and d–f) P3HT coated by 1 g L^{-1} CN6-CP$^{\bullet-}$NBu$_4^+$ ethanol solution.

property, which is affected by the doping process—redox-induced changes of the chemical potential of a semiconductor.[33] Bare silicon substrates covered by thick silica layers exhibit SPs in the +600 to +800 mV range, which corresponds to a work function (WF) of –5.0 to 5.2 eV, a typical value reported in literature for SiO_2.[33b] Pristine P3HT layers deposited onto these substrates have SPs of about ≈+200 mV, corresponding to WF of ≈–4.6 eV, which compares well with the literature data.[34] As a representative example, **Figure 7**a–c shows topographic and SP images of a 12 nm thick P3HT film. Figure 7d–f shows topography and FM-KPFM images

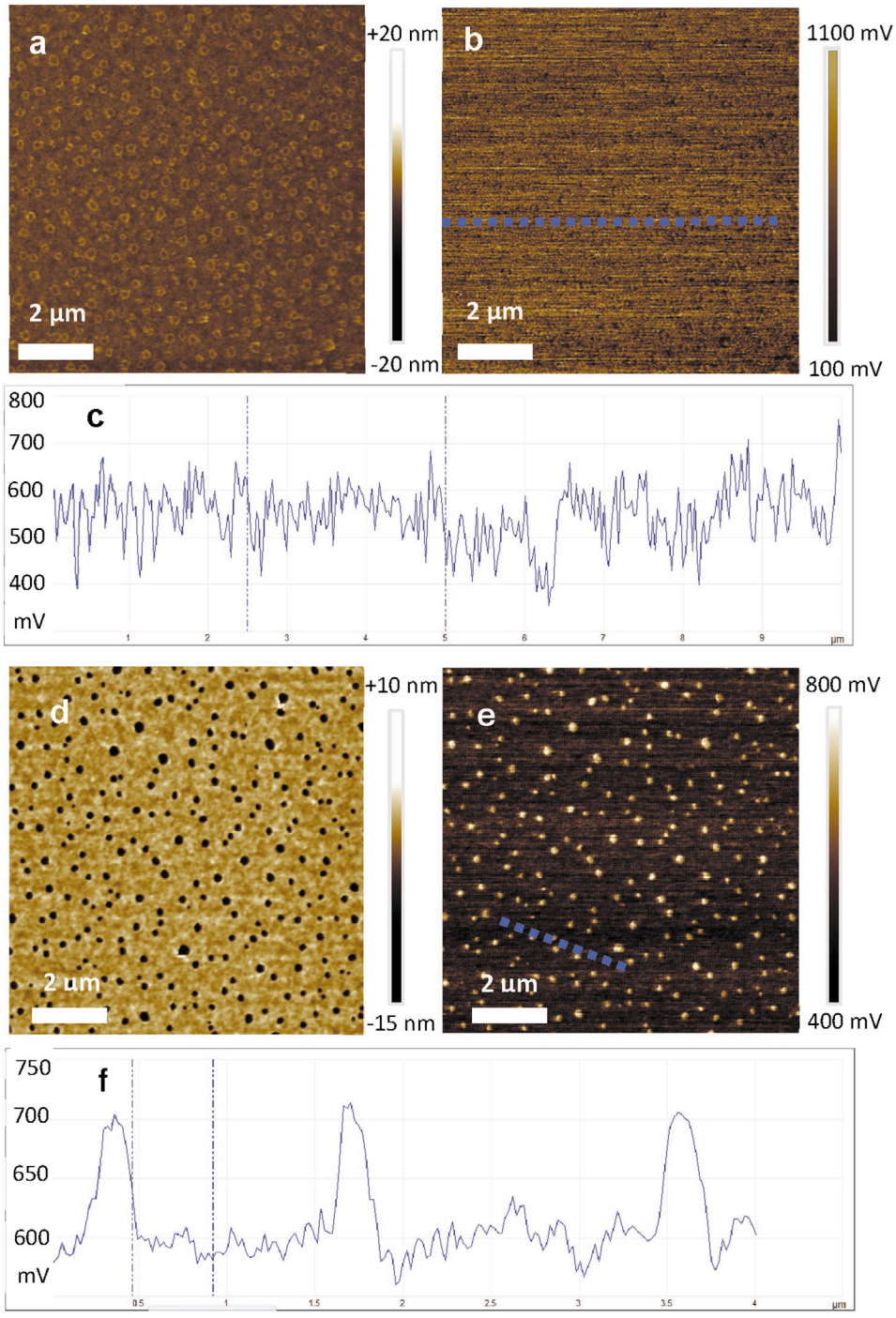

Figure 8. a,d) AFM topography, b,e) SP images and c,f) corresponding SP profiles of the MxS-doped film (MDR = 0.3) and the same after washing with ethanol.

of SqP-doped P3HT/CN6-CP$^{\bullet-}$NBu$_4^+$ films prepared at 1 g L^{-1} dopant concentration. Elongated crystallites and round-shaped particles seen in the topography and SP images and having an SP of ≈+750 mV, represent the dopant, whereas the background, having an SP of ≈+380 mV, corresponds to a slightly doped P3HT. The latter conclusion comes from a comparison of undoped P3HT SP (≈+200 mV) and strongly doped P3HT, prepared by the MxS method (≈+600 mV, **Figure 8**b,c).

The fact that the SP of the background area in Figure 7e falls between the SPs of the undoped and heavily doped P3HT suggests that the dopant does not mix extensively with P3HT in the case of SqP method as it does for the MxS approach.

It is also interesting to compare morphology and SP images of the films doped by the two methods. As seen from Figure 8a, MxS films contain a number of round-shaped blobs, 100–200 nm in diameter, which are separated from each other

by a distance of 1–3 µm. These objects are not seen on the SP image and the whole surface has the SP of ≈+600 mV (–5.0 eV), which is close to the WF of the dopant. Interesting transformations were found upon the rinsing of the sample with ethanol, which is a selective solvent for the dopant. As seen from Figure 8d,f, this procedure led to the formation of holes in places of the round-shaped objects. According to the SP data, the material under the holes is silica, whereas the background having unchanged SP upon rinsing, represents a doped P3HT. Obviously, the rinsing procedure removes the round-shaped dopant clusters forming holes revealing the bare silica (bright objects in Figure 8f with SP ≈+700 mV, WF –5.1 eV).

At the same time, the dopant entrapped inside the polymer film (background in Figure 8f) remains unwashed upon the rinsing. This follows from the fact that the SP of the background coincides with the SP of the doped P3HT (≈+600 mV) but not with the SP of undoped P3HT (≈+200 mV).

2.4. Grazing Incidence Wide Angle X-Ray Scattering (GIWAXS) Studies

GIWAXS was used in the present work to evaluate the effect of the dopant molecules on the structure of the films prepared by different methods. Previously, we reported structural data for CN6-CP$^{\bullet-}$NBu$_4^+$-doped P3HT thin films prepared by the MxS method.[29b] We showed that the blending of the polymer with CN6-CP$^{\bullet-}$NBu$_4$ does not reduce, but even slightly increases crystallinity of P3HT. However, the most prominent change is a significant increase of the lamellar spacing from 16.44 Å for pristine P3HT to 17.84 Å for the MxS-doped one along with a slight decrease of the π-stacking distance. This rearrangement of the structure was tentatively attributed to incorporation of dopant molecules between alkyl chains,[29b] which corroborates with other reports.[16] In the present work, we extend these studies by measuring SqP-doped P3HT/CN6-CP$^{\bullet-}$NBu$_4^+$ and P3HT/PDADMAC/CN6-CP$^{\bullet-}$K$^+$ films (the latter system was investigated in our previous paper, however structural studies were not reported). **Table 1** compares relative crystallinity, coherence length, lamellar spacing, and π-staking distance for the films obtained by the three methods (see the Experimental Section for the calculation details).

The overall crystallinity underwent an increase in the MxS-doped films (67.4–76.5%), compared to pristine P3HT (62.3%) and a minor decrease in SqP-films doped by CN6-CP$^{\bullet-}$NBu$_4^+$ (59.0–60.9%). The crystallinity of the P3HT/PDADMAC/CN6-CP$^{\bullet-}$K$^+$ films is also decreased compared to undoped P3HT. The size of crystalline P3HT domains (coherence length) underwent rather minor changes upon doping: being equal to 8.8 nm for pristine P3HT, it ranges from 7.7 to 10.1 nm for the films doped by different methods. In general, the observed variations of the relative crystallinity and coherence length are rather minor and most probably could not explain the difference in conductivity of the doped films produced by the three methods. The most significant change in GIWAXS patterns is a doping-induced increase of the lamellar spacing from 16.4 Å for pristine P3HT to 17.6 Å for the MxS-doped film, 17.8 Å for the SqP-doped P3HT/CN6-CP$^{\bullet-}$NBu$_4^+$, and 18.1 Å for the P3HT/PDADMAC/CN6-CP$^{\bullet-}$K$^+$ (**Figure 9**). These changes are accompanied by a slight decrease of the π-stacking distance from 3.77 nm for pristine P3HT to 3.67 Å, e.g., for the P3HT/PDADMAC/CN6-CP$^{\bullet-}$K$^+$. The deposition of the polycation interlayer (which is an intermediate step in the fabrication of the P3HT/PDADMAC/CN6-CP$^{\bullet-}$K$^+$ films) did not change the molecular arrangement of pristine P3HT, emphasizing the key role of the dopant in the restructuring.

In general, doping-induced structural changes found in this work corroborate well with observations, reported previously. For example, for the P3HT/F4TCNQ system, an increase of the periodicity from 16.5 to 18.1 Å and a decrease of the π-staking distance from 3.76 to 3.69 Å upon doping, were reported (Figure 9d).[16,35,36a,b] Along the same line, Moule et al. demonstrated both experimentally and theoretically that the doping induced spacing change is a result of a flattening of P3HT side chains.[36c] Similarly, the doping of P3HT in iodine vapors led to increase of the lamellar spacing from 16.6 to 18.5 Å, as proposed in early works of Tashiro et al.[37] The observed enlargement of the lamellar spacing was attributed to incorporation of the dopant into the polymer side groups (Figure 8d). However, the most surprising finding of the present work is that abovementioned structural transformations are observed not only in MxS-doped films, where the polymer and the dopant are intermixed, but also in those SqP samples, in which the constituting components differ strongly by their polarity, which were deposited from strongly orthogonal solvents and which are believed to

Table 1. Lamellar spacing, d_{100}, π–π stacking distance, d_{020}, and relative crystallinity of the P3HT polymer of the different films prepared by the three different methods.

Film	d_{100} [Å]	d_{020} [Å]	Relative crystallinity [%]	Coherence length [Å]
# 1: P3HT	16.44	3.77	62.3	87.6
# 2: MxS-P3HT&CN6-CP$^{\bullet-}$NBu$_4^+$(2/1)	17.59	3.75	76.5	77.2
# 3: MxS-P3HT&CN6-CP$^{\bullet-}$NBu$_4^+$(3/1)	17.31	3.72	67.4	82.2
# 4: SqP-P3HT/CN6-CP$^{\bullet-}$NBu$_4^+$(10 g L^{-1})	17.84	3.69	59.0	94.5
# 5: SqP-P3HT/CN6-CP$^{\bullet-}$NBu$_4^+$(1 g L^{-1})	17.60	3.68	60.9	94.5
# 6: SqP-P3HT(60 nm)/PDADMAC	16.46	3.80	57.2	92.4
# 7: SqP-P3HT(60 nm)/PDADMAC/CN6-CP$^{\bullet-}$K$^+$	18.01	3.69	62.2	91.8
# 8: SqP-P3HT(20 nm)/PDADMAC	16.53	3.76	59.5	100.5
# 9: SqP-P3HT(20 nm)/PDADMAC/CN6-CP$^{\bullet-}$K$^+$	18.12	3.69	62.3	86.7

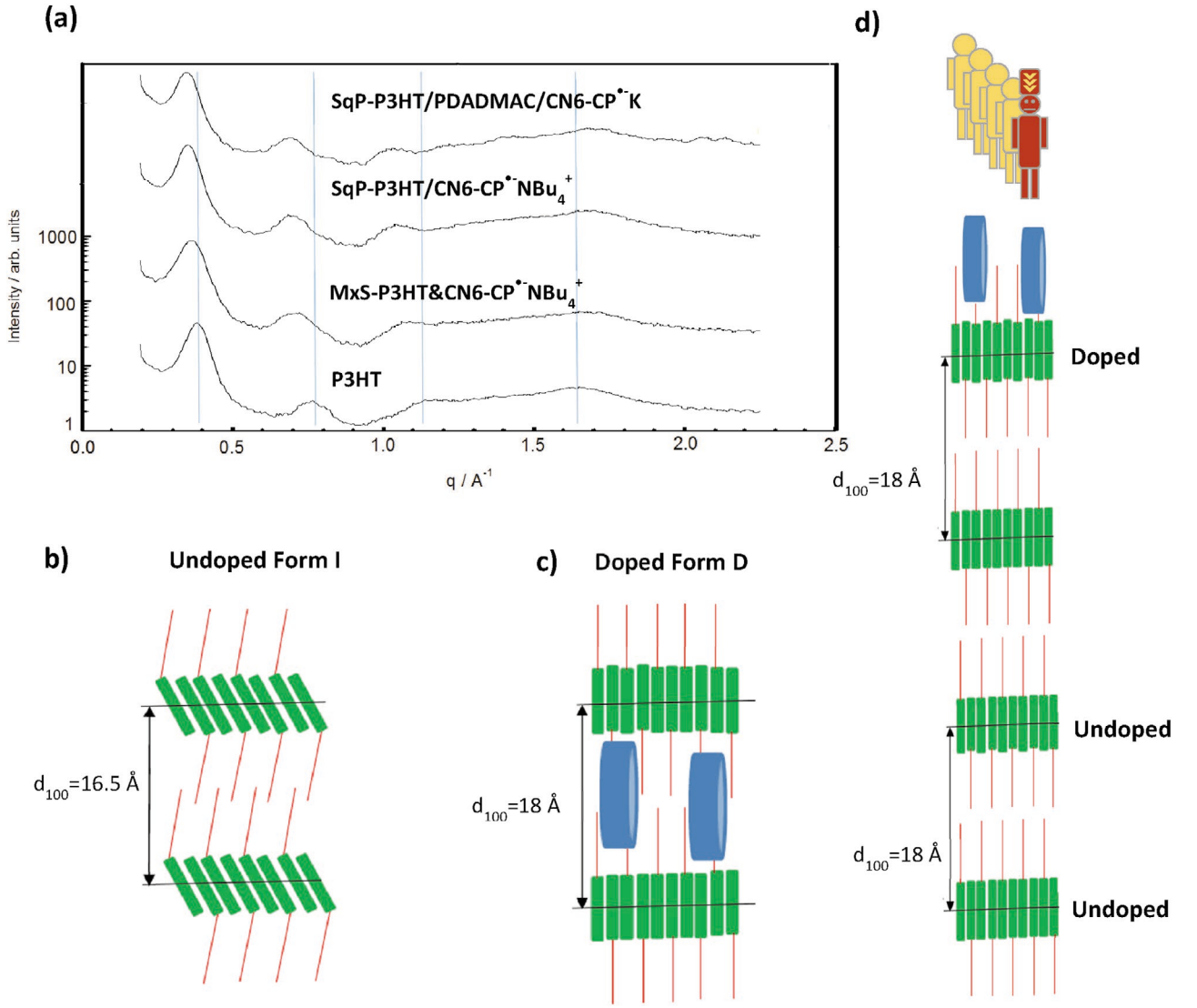

Figure 9. a) Radial integration of the GIWAXS patterns of the various films prepared as described in legends; the vertical lines in (a) correspond to the main peaks of P3HT Form I. Schematic representation of possible arrangements for P3HT: b) the well-established Form I for undoped P3HT; c) a doped Form D with the dopant intercalated into side groups inherent for MxS-doping method, according to Brinkmann and co-workers[35]. Illustration of the "Sergeants-and-Soldiers Principle" for SqP-doping of P3HT: d) the topmost P3HT layer with intercalated dopant has a conventional doped Form D, whereas the bottom layer adopt the same arrangement without intercalated dopant.

be spatially separated in the resulting films. For example, very similar lamellar spacings are observed in P3HT films coated by a concentrated (10 g L^{-1}) solution of CN6-CP$^{\bullet-}NBu_4^+$ in ethanol as well as by a diluted solution (1 g L^{-1}) (Table 1, entries 4 and 5, respectively). Taking into account that according to AFM (Figure 3), the former sample is fully covered with the dopant, whereas the latter sample is covered only partly, the similarity of the spacing demonstrates that even minor amounts of the dopant are able to induce deep structural transformations. The fact that the enlargement of the lamellar spacing does not necessarily require the incorporation of the dopant inside the P3HT phase, but it occurs also at interfacial contact of the polymer and the dopant is especially obvious in the example of the SqP-P3HT/PDADMAC/CN6-CP$^{\bullet-}K^+$ film. Indeed, the SqP preparation of this sample involves the coating from a water-soluble dopant, which is immiscible with the polymer so that its infiltration into the bulk of the strongly hydrophobic polymer is very unlikely, as shown in our previous paper.[28] Despite this, the SqP-P3HT/PDADMAC/CN6-CP$^{\bullet-}K^+$ film shows the largest spacing of 18.1 Å (Table 1, entry 9). At first sight, these data contradict with the bilayered structure of the doped SqP films and rather suggest intercalation of the dopant between alkyl side groups, similarly to the MxS films. However, it is important to note that the only information related to the structure of P3HT could be unambiguously extracted from X-ray measurement, as this component is crystalline, whereas the structural information about dopants, which are amorphous when blended with polymers, is the subject of extensive speculations. For example, for MxS films, Chabinyc and co-workers proposed that F4TCNQ cocrystallizes in a cofacial manner with a polymer (PBTTT, in

that case).[24] For SqP-doped films, Moule and co-workers proposed that the dopant intercalates into the amorphous part of P3HT.[30] Schwartz and co-workers[16] and Brinkmann and co-workers[35] criticized the idea of the π-stacked P3HT$^+$:F4TCNQ$^-$ cocrystals being the dominant structure for any kinds of doping. Instead, they suggested that the dopant molecules, which account for the conductivity enhancement in SqP films, intercalate between the alkyl side chains of P3HT crystals.[35,36] The same arrangement was proposed for SqP P3HT films doped from vapor phase.[38] In general, this model assumes a doping-induced transformation of the thermodynamically stable Form I[39] (Figure 9c) for undoped P3HT in which the polymer side chains are significantly tilted relative to the conjugated backbone plane, into the structure with the side chains essentially coplanar with the backbone (let us call this structure Form D). The latter structure accounts for the enlargement of the lamellar spacing and explains the incorporation of the dopant. Regarding the structure of the doped films, an interesting feature is that the lamellar spacing in doped P3HT does not exceed the value of 18.0–18.5Å even at high doping ratios. This suggests that the maximal spacing is defined by the length of alkyl side groups oriented normally to the polymer backbone (Figure 9d), but not the volume requirements of the intercalated dopant. Clearly, this configuration allows a limited uptake of the dopant but other arrangements, in which adjacent P3HT molecules are not closely packed and provide more space to accommodate the dopant, are never observed experimentally. As another extreme, we postulate the formation, under certain circumstances, of the Form D completely without incorporation of the dopant, as shown in Figure 9d. The existence of this form was experimentally observed by Brinkmann and co-workers who reported TEM investigations of P3HT films aligned by a rubbing technique and then sequentially doped by F4TCNQ. For the lowest concentration of the dopant, they particularly reported that the fraction of undoped P3HT is not represented with the pristine undoped Form I but is "... attributed to undoped P3HT chain segments within the crystals of the doped phase."[35] This model also explains the observations in our work. For the P3HT/CN6-CP$^{\bullet-}$NBu$_4^+$ system, we suggest that the enlargement of the lamellar spacing does not necessarily occur due to the incorporation of the dopant into the P3HT crystal as shown in Figure 9d, but can also be a result of a so-called "Sergeants-and-Soldiers Principle."[40] It was introduced to describe conformation transitions in helical polymers according to which, it is required to add a small portion of chiral units (sergeants) to the achiral units (soldiers) to favor one helical sense of the polymer. In our case, the topmost P3HT layer having increased lamella spacing because of intercalation of dopant molecules (Figure 9e, top), acts as sergeants that force the same structure in many bottom P3HT layers (soldiers), although they have no incorporated dopants (Figure 9f, bottom).

2.5. Absorption Spectroscopy

We now shift our focus to the optical properties of the doped P3HT/CN6-CP$^{\bullet-}$NBu$_4^+$ films prepared by MxS and SqP techniques. **Figure 10** compares UV–vis–IR absorption spectra of

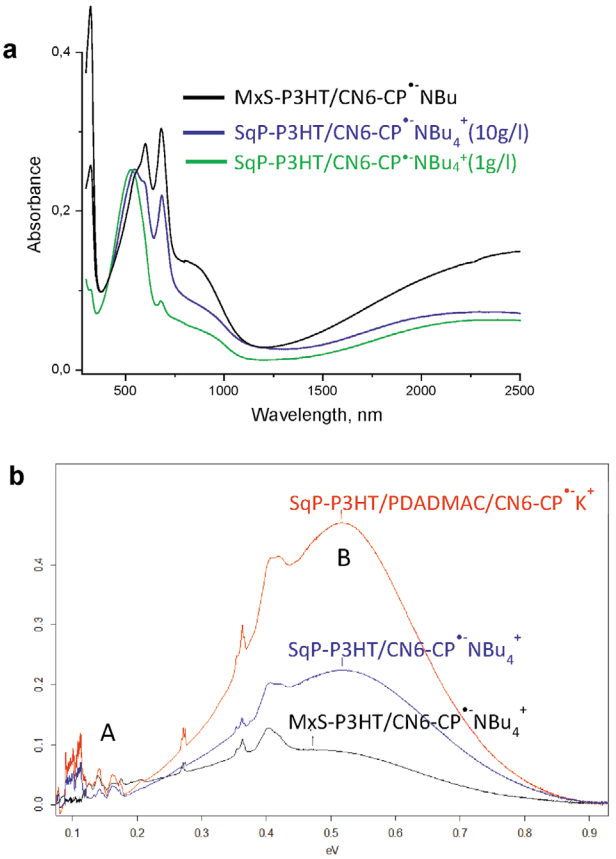

Figure 10. a) UV–vis–NIR absorption spectra of SqP-P3HT/CN6-CP$^{\bullet-}$NBu$_4^+$ (10 g L^{-1}) (blue line), SqP-P3HT/CN6-CP$^{\bullet-}$NBu$_4^+$ (1 g L^{-1}) (green line), and MxS-P3HT&CN6-CP$^{\bullet-}$NBu$_4^+$ (black line) films. b) Fourier-transform infrared (FTIR) spectra of MxS-P3HT&CN6-CP$^{\bullet-}$NBu$_4^+$ (black line), SqP-P3HT/CN6-CP$^{\bullet-}$NBu$_4$ (blue line), and SqP-P3HT/PDADMAC/CN6-CP$^{\bullet-}$K$^+$ (red line) films.

the doped P3HT/CN6-CP$^{\bullet-}$NBu$_4^+$ films on glass slides prepared by MxS method (black) and SqP technique at different concentrations, of 1 g L^{-1} (green) and 10 g L^{-1} (blue). To facilitate interpretation of the data, we prepared films having approximately the same P3HT content. To fulfill this requirement, P3HT layers in SqP samples are two times thinner than the MxS sample, (≈20 nm vs ≈40 nm), as the polymer content in the MxS sample is 50%. The first observation is that both SqP samples are doped to a smaller degree, which follows from much stronger absorptions of the neutral polymer at λ_{max} = 520 nm and a lower polaron absorption above 2000 nm in these samples, compared to the MxS-doped sample. This corroborates with the layered structure of the sequentially processed films, so that significant parts of 20 nm thick P3HT films in both SqP samples remained undoped. An important conclusion comes from a comparison of the light absorption and conductivity data. Despite lower polaron absorptions in SqP-doped samples, they have higher conductivity than the MxS-doped samples (e.g., compare entries 4 and 16 in Table S1 in the Supporting Information), highlighting the higher efficiency of the SqP-doping method.

Figure 10b compares the IR region of the absorption spectra of ≈5 nm thick films prepared by different doping techniques.

For technical reasons (too strong polaron absorptions), the measurements of thicker films was not possible. The first observation is that the spectra of the two SqP samples, i.e., SqP-P3HT/CN6-CP$^{\bullet-}$NBu$_4^+$ and SqP-P3HT/PDADMAC/CN6-CP$^{\bullet-}$K$^+$, are very similar but the last one has a much higher intensity. However, both of these spectra differ significantly from the samples produced by the MxS method. Particularly, the maximum of peak B, corresponding to the conventional intrachain polaron transition of the MxS sample, is clearly redshifted relative to the peak maxima of both SqP-P3HT/CN6-CP$^{\bullet-}$NBu$_4^+$ and SqP-P3HT/PDADMAC/CN6-CP$^{\bullet-}$K$^+$ samples (0.405 eV vs 0.524 and 0.522 eV, respectively).[17,41] The redshift of the intrachain polaron absorption band in the MxS sample film corroborates with a somewhat higher crystalline order in this sample compared to the SqP samples (see GIWAXS data). Interestingly, the so-called peak A, which usually appears in the 0.1–0.15 eV region and overlaps with IR-active vibration (IRAV) signals, is negligible in the MxS sample. This low energy absorption is usually attributed to a portion of polarons, which are delocalized over several polymer chains. As a rule, this low energy absorption is more pronounced in samples with higher crystallinity (and a more redshifted peak B). Quite unexpectedly, the less crystalline SqP samples having relatively blue shifted peaks B possess significantly more intense peaks in the IRAVs region. Although the exact reason for this discrepancy is not clear, the appearance of the peak A in the less crystalline SqP samples may be attributed to the layered morphology of the SqP samples, which favors the interchain delocalization of polarons. This statement corroborates also with the highest intensity of the polaron absorption in the peak B region of the infrared spectra for the SqP-P3HT/PDADMAC/CN6-CP$^{\bullet-}$K$^+$ sample, which has the most well-defined layered structure.

3. Summary and Conclusions

In this paper, by using CN6-CP$^{\bullet-}$NBu$_4^+$ as the dopant and P3HT as model semiconductor, we compared the efficiency of the two doping methods—MxS and SqP. MxS films show moderate conductivity of ≈0.1 S cm^{-1} in a broad range of thickness. In contrast, the conductivity of SqP films exhibits a strong thickness dependency, the highest value of 3–7 S cm^{-1} was achieved for thinner (1.5–5 nm) films, whereas it drops two orders of magnitudes for 100 times thicker films. The MxS films exhibit a bulk doping with a more or less homogeneous distribution of the dopant in the P3HT films, which results in thickness-independency of the conductivity. The results with the SqP films are explained in terms of an interfacial doping mechanism, according to which, only the layers close to the P3HT/dopant interface are doped efficiently, whereas internal P3HT layers remain essentially undoped. TEM, AFM, and KPFM investigations confirm the layered structure and, within resolutions inherent to these methods, exclude intercalation of the dopant in substantial amounts. It should be, however, stated that none of the methods allows detection of traces of the dopant inside the P3HT phase, so penetration of some minor amounts of the dopant into the semiconductor cannot be excluded. This is in contrast to the previously investigated P3HT/F4TCNQ system, where the dopant intercalates significantly into the polymer phase. It is believed that the layered structure of the doped films originates from a strong difference in polarities of the dopant and the semiconductor polymer, as well as from the fact that an orthogonal solvent was used for the deposition of the dopant. GIWAXS and FTIR measurements demonstrated that the low conductivity of the MxS-doped films in the ultrathin film regime is not due to a lower molecular order in these films. On the contrary, MxS-doped samples show even slightly higher crystallinity than the SqP ones. Furthermore, both deposition methods result in a very similar molecular packing with increased lamellar spacing of ≈18 Å, characteristic to the MxS-doped state. We propose that the difference in the charge transport lies on the macroscale. Indeed, AFM reveals a number of sub-micrometer clusters of the phase-separated dopant in the MxS film, which can prohibit transport of charges at large, multi-micrometer distances. The temperature-dependent charge transport measurements reveal a lower activation energy for the charge carriers in the SqP compared to the MxS samples (79 meV vs 110 meV), suggesting that at a given temperature, SqP films have higher charge carrier concentration, which could also be a reason for the higher conductivity. The fact that a higher polaron absorption and hence higher concentration of ionized states was observed in MxS samples (in comparison to SqP) indicates that a majority of the transferred charges are trapped leading to the lower conductivity.

4. Experimental Section

Materials: CN6-CP$^{\bullet-}$NBu$_4^+$ was synthesized as described in ref. [29a]. P3HT batch I (M_n = 28 kg mol^{-1}; M_w = 39 kg mol^{-1}) was synthesized as previously described.[42] P3HT batch II (M_n = 46 kg mol^{-1}; M_n = 83 kg mol^{-1}) was purchased from Merck and fractionalized by Soxhlet extraction (chloroform fraction was used). Solvents (chlorobenzene, chloroform, and ethanol) were purchased from Merck.

GIWAXS Measurements: GIWAXS measurements were performed using a Ganesha 300XL+ Instrument (SAXSLAB ApS, Lyngby/Denmark) with a Cu X-ray source operated at 50 kV/0.6 mA (λ = 1.5408 Å), and a three-slit collimation system. A 2D Pilatus 300 K detector was used at 110 mm sample to detector distance and an incident angle of 0.2°. The data were analyzed using GIXSGUI program. The relative degree of crystallinity, χ, and lamellar spacing were calculated from radially integrated line profiles of the GIWAXS patterns between $\phi = 0°$ and $\phi = 90°$. The resulting curve was fitted using individual Gaussian functions for each peak and the amorphous broad hump extending between q = 1.1 to 2.2 Å^{-1} superimposed on a linear background. χ values were obtained from the ratio of the total scattering intensity of the (100) peak to that of the sum of the total scattering intensities of the amorphous hump and the (100) peak. The lamellar spacing and coherence length were calculated from the (100) peak position, q_{100}, and the full width at half maximum, Δq_{100} according to following equations: $d_{100} = \frac{2\pi}{q_{100}}$ and coherence length $= \frac{2\pi}{\Delta q_{100}}$, respectively.

Preparation of Samples for Electrical Characterizations: To prepare SqP samples, P3HT solutions in chloroform were deposited by spin-coating onto freshly cleaned devices for electrical measurements. Coating parameters (concentrations and rotation speed) were adjusted experimentally to achieve desirable thicknesses. For example, the thinnest, ≈1.5 nm, P3HT film is formed by spin-coating of 0.5 g L^{-1} in chlorobenzene at 3000r^{-1}; spin-coating of 5 g L^{-1} chlorobenzene solution at 2000r^{-1} gives ≈20 nm thick P3HT film. The thicknesses were determined by both ellipsometry and AFM scratch test measurements, as described in detail in the Supporting Information of the previous

paper.[28] On the second step, a few drops of 10 g L^{-1} solution of the dopant in ethanol were deposited atop of respective P3HT films to fully cover them with the dopant solution, which were removed by immediate switching on spin-coater at 2000r^{-1}. For the MxS method, P3HT and the dopant were codissolved in chloroform to get desirable MDRs and deposited onto freshly cleaned devices for electrical measurements by using spin-coating. Coating parameters (concentrations and rotation speed) were chosen to achieve desirable film thickness.

Electrical Characterization: Highly doped silicon wafers with 300 nm SiO_2 were used as substrates. For the electrodes, 2 nm Cr and 50 nm Au were thermally evaporated through a shadow mask at a vacuum of ≈10^{-7} mbar. The electrodes had a width of 4.5 and 11 mm and the distance between two electrodes was 200 and 300 µm, respectively. For the current–voltage (*IV*) measurement, a manual probe station (Cascade Microtech GmbH) and a Keysight B1500A Semiconductor Device Parameter Analyzer were used. *IV* sweeps for voltages of 0–10 V were performed for each substrate (3 sweeps). The linear current–voltage dependencies were extracted and the resistance of each sample was calculated due to Ohm's law (Equation (1))

$$R = \frac{U}{I} \tag{1}$$

From the resistance, the conductivity of the film was calculated based on Pouillet's law (Equation (2))

$$\sigma = \frac{1}{\rho} = \frac{l}{RA} = \frac{l}{Rtw} \tag{2}$$

where ρ is the resistivity, l is the distance between two electrodes, t is the thickness of the doped film, and w is the width of the electrodes. The exact distances between two electrodes were measured for every sample with optical microscopy.

Supporting Information

Supporting Information is available from the Wiley Online Library or from the author.

Acknowledgements

The authors gratefully acknowledge support from the Deutsche Forschungsgemeinschaft (DFG) (Grant KI-1094/9-1) and the Cluster of Excellence (EXC 1056) "Center for Advancing Electronics Dresden (cfaed)." T.B. gratefully acknowledges financial support by the Russian Foundation for Basic Research (Project 18-03-00715). Y.K., B.D., and M.B. acknowledge the financial support from the German Research Foundation (DFG) through KR 4364/4-1. M.A.-H. thanks the University of Jordan and Leibniz-Institut für Polymerforschung, Dresden (IPF) for financial support.

Conflict of Interest

The authors declare no conflict of interest.

Keywords

conductivity, interfacial doping, organic semiconductors, p-doping, solution-processable organic devices

Received: December 3, 2019
Revised: February 3, 2020
Published online: April 13, 2020

[1] A. Facchetti, *Chem. Mater.* **2011**, *23*, 733.
[2] B. Lüssem, M. Riede, K. Leo, *Phys. Status Solidi A* **2013**, *210*, 9.
[3] I. E. Jacobs, A. J. Moulé, *Adv. Mater.* **2017**, *29*, 1703063.
[4] G. Lu, J. Blakesley, S. Himmelberger, P. Pingel, J. Frisch, I. Lieberwirth, I. Salzmann, M. Oehzelt, R. Di Pietro, A. Salleo, N. Koch, D. Neher, *Nat. Commun.* **2013**, *4*, 1588.
[5] R. Di Pietro, T. Erdmann, N. Wang, X. Liu, D. Gräfe, J. Lenz, J. Brandt, D. Kasemann, K. Leo, M. Al-Hussein, K. L. Gerasimov, D. Doblas, D. A. Ivanov, B. Voit, D. Neher, A. Kiriy, *J. Mater. Chem. C* **2016**, *4*, 10827.
[6] J. Panidi, A. F. Paterson, D. Khim, Z. Fei, Y. Han, L. Tsetseris, G. Vourlias, P. A. Patsalas, M. Heeney, T. D. Anthopoulos, *Adv. Sci.* **2018**, *5*, 1700290.
[7] N. Shin, J. Zessin, M. H. Lee, M. Hambsch, S. C. B. Mannsfeld, *Adv. Funct. Mater.* **2018**, *28*, 1802265.
[8] S. Reineke, F. Lindner, G. Schwartz, N. Seidler, K. Walzer, B. Lüssem, K. Leo, *Nature* **2009**, *459*, 234.
[9] Y. Zhang, H. Zhou, J. Seifter, L. Ying, A. Mikhailovsky, A. J. Heeger, G. C. Bazan, T.-Q. Nguyen, *Adv. Mater.* **2013**, *25*, 7038.
[10] A. M. Glaudell, J. E. Cochran, S. N. Patel, M. L. Chabinyc, *Adv. Energy Mater.* **2015**, *5*, 1401072.
[11] AMOLED - introduction and market status, https://www.oled-info.com/amoled (accessed: April 2020).
[12] M. C. Gather, A. Köhnen, A. Falcou, H. Becker, K. Meerholz, *Adv. Funct. Mater.* **2007**, *17*, 191.
[13] a) S. Ho, S. Liu, Y. Chen, F. So, *J. Photonics Energy* **2015**, *5*, 057611; b) J. Perelaer, P. J. Smith, D. Mager, D. Soltman, S. K. Volkman, V. Subramanian, J. G. Korvink, U. S. Schubert, *J. Mater. Chem.* **2010**, *20*, 8446.
[14] G. Zuo, O. Andersson, H. Abdalla, M. Kemerink, *Appl. Phys. Lett.* **2018**, *8*, 112.
[15] D. T. Scholes, S. A. Hawks, P. Y. Yee, H. Wu, J. R. Lindemuth, S. H. Tolbert, B. J. Schwartz, *J. Phys. Chem. Lett.* **2015**, *6*, 4786.
[16] D. T. Scholes, P. Y. Yee, J. R. Lindemuth, H. Kang, J. Onorato, R. Ghosh, C. K. Luscombe, F. C. Spano, S. H. Tolbert, B. J. Schwartz, *Adv. Funct. Mater.* **2017**, *27*, 1702654.
[17] A. R. Chew, R. Ghosh, Z. Shang, F. C. Spano, A. Salleo, *J. Phys. Chem. Lett.* **2017**, *8*, 4974.
[18] I. Salzmann, G. Heimel, M. Oehzelt, S. Winkler, N. Koch, *Acc. Chem. Res.* **2016**, *49*, 370.
[19] a) E. F. Aziz, A. Vollmer, S. Eisebitt, W. Eberhardt, P. Pingel, D. Neher, N. Koch, *Adv. Mater.* **2007**, *19*, 3257; b) K.-H. Yim, G. L. Whiting, C. E. Murphy, J. J. M. Halls, J. H. Burroughes, R. H. Friend, J.-S. Kim, *Adv. Mater.* **2008**, *20*, 3319; c) D. T. Duong, C. Wang, E. Antono, M. F. Toney, A. Salleo, *Org. Electron.* **2013**, *14*, 1330.
[20] P. K. Koech, A. B. Padmaperuma, L. Wang, J. S. Swensen, E. Polikarpov, J. T. Darsell, J. E. Rainbolt, D. J. Gaspar, *Chem. Mater.* **2010**, *22*, 3926.
[21] Z. Q. Gao, B. X. Mi, G. Z. Xu, Y. Q. Wan, M. L. Gong, K. W. Cheah, C. H. Chen, *Chem. Commun.* **2008**, *44*, 117.
[22] O. Solomeshch, Y. J. Yu, A. A. Goryunkov, L. N. Sidorov, R. F. Tuktarov, D. H. Choi, J.-I. Jin, N. Tessler, *Adv. Mater.* **2009**, *21*, 4456.
[23] Y. Qi, T. Sajoto, S. Barlow, E. G. Kim, J. L. Bredas, S. R. Marder, A. Kahn, *J. Am. Chem. Soc.* **2009**, *131*, 12530.
[24] J. E. Cochran, M. J. N. Junk, A. M. Glaudell, P. L. Miller, J. S. Cowart, M. F. Toney, C. J. Hawker, B. F. Chmelka, M. L. Chabinyc, *Macromolecules* **2014**, *47*, 6836.
[25] P. Pingel, R. Schwarzl, D. Neher, *Appl. Phys. Lett.* **2012**, *100*, 143303.
[26] A. Dai, Y. Zhou, A. L. Shu, S. K. Mohapatra, H. Wang, C. Fuentes-Hernandez, Y. Zhang, S. Barlow, Y.-L. Loo, S. R. Marder, B. Kippelen, A. Kahn, *Adv. Funct. Mater.* **2014**, *24*, 2197.
[27] J. Li, C. W. Rochester, I. E. Jacobs, S. Friedrich, P. Stroeve, M. Riede, A. J. Moulé, *ACS Appl. Mater. Interfaces* **2015**, *7*, 28420.

[28] Y. Karpov, N. Kiriy, P. Formanek, J. Zessin, M. Hambsch, S. C. B. Mannsfeld, F. Lissel, T. Beryozkina, V. Bakulev, B. Voit, A. Kiriy, *ACS Appl. Mater. Interfaces* **2019**, *11*, 4159.

[29] a) Y. Karpov, T. Erdmann, I. Raguzin, M. Al-Hussein, M. Binner, U. Lappan, M. Stamm, K. L. Gerasimov, T. Beryozkina, V. Bakulev, D. V. Anokhin, D. A. Ivanov, F. Günther, S. Gemming, G. Seifert, B. Voit, R. Di Pietro, A. Kiriy, *Adv. Mater.* **2016**, *28*, 6003; b) Y. Karpov, N. Kiriy, M. Al-Hussein, M. Hambsch, T. Beryozkina, V. Bakulev, S. C. B. Mannsfeld, B. Voit, A. Kiriy, *Chem. Commun.* **2018**, *54*, 307.

[30] I. E. Jacobs, E. W. Aasen, J. L. Oliveira, T. N. Fonseca, J. D. Roehling, J. Li, G. Zhang, M. P. Augustine, M. Mascal, A. Moule, *J. Mater. Chem. C* **2016**, *4*, 3454.

[31] V. A. Kolesov, C. Fuentes-Hernandez, W.-F Chou, N. Aizawa, F. A. Larrain, M. Wang, A. Perrotta, S. Choi, S. Graham, G. C. Bazan, T.-Q. Nguyen, S. R. Marder, B. Kippelen, *Nat. Mater.* **2017**, *16*, 474.

[32] Application Note #140: PeakForce Kelvin Probe Force Microscopy, https://www.bruker.com/fileadmin/user_upload/8-PDF-Docs/SurfaceAnalysis/AFM/ApplicationNotes/AN140-RevA1-PeakForce_KPFM-AppNote.pdf (accessed: April 2020).

[33] a) Y. Krupskaya, I. Gutiérrez Lezama, A. F. Morpurgo, *Adv. Funct. Mater.* **2016**, *26*, 2334; b) A. Liscio, V. Palermo, O. Fenwick, S. Braun, K. Müllen, M. Fahlman, F. Cacialli, P. Samorì, *Small* **2011**, *7*, 634.

[34] M. Baghgar, M. D. Barnes, *ACS Nano* **2015**, *9*, 7105.

[35] A. Hamidi-Sakr, L. Biniek, J.-L. Bantignies, D. Maurin, L. Herrmann, N. Leclerc, P. Lévêque, V. Vijayakumar, N. Zimmermann, M. Brinkmann, *Adv. Funct. Mater.* **2017**, *27*, 1700173.

[36] a) J. Hynynen, D. Kiefer, Li. Yu, R. Kroon, R. Munir, A. Amassian, M. Kemerink, C. Müller, *Macromolecules* **2017**, *50*, 8140; b) J. Hynynen, D. Kiefer, C. Müller, *RSC Adv.* **2018**, *8*, 1593; c) T. F. Harrelson, Y. Q. Cheng, J. Li, I. E. Jacobs, A. J. Ramirez-Cuesta, R. Faller, A. J. Moulé, *Macromolecules* **2017**, *50*, 2424.

[37] K. Tashiro, M. Kobayashi, T. Kawai, K. Yoshino, *Polymer* **1997**, *38*, 2867.

[38] a) E. Lim, K. A. Peterson, G. M. Su, M. L. Chabinyc, *Chem. Mater.* **2018**, *30*, 998; b) K. Kang, S. Watanabe, K. Broch, A. Sepe, A. Brown, I. Nasrallah, M. Nikolka, Z. Fei, M. Heeney, D. Matsumoto, K. Marumoto, H. Tanaka, S.-I. Kuroda, H. Sirringhaus, *Nat. Mater.* **2016**, *15*, 896.

[39] T. J. Prosa, M. J. Winokur, R. D. McCullough, *Macromolecules* **1996**, *29*, 3654.

[40] M. M. Green, N. C. Peterson, T. Sato, A. Teramoto, R. Cook, S. Lifson, *Science* **1995**, *268*, 1860.

[41] R. Ghosh, A. R. Chew, J. Onorato, V. Pakhnyuk, C. K. Luscombe, A. Salleo, F. C. Spano, *J. Phys. Chem. C* **2018**, *122*, 18048.

[42] R. S. Loewe, P. C. Ewbank, J. Liu, L. Zhai, R. D. McCullough, *Macromolecules* **2001**, *34*, 4324.